

Record Stability for Fully Passive Perovskite-Based X-Ray Detectors Through the Use of Starch as Templating Agent

Matteo Verdi, Antonella Giuri, Andrea Ciavatti, Aurora Rizzo, Carola Esposito Corcione, Laura Basiricò, Silvia Colella,* and Beatrice Fraboni*

High sensitivity and efficient X-ray detectors are needed to promote and boost their application as tools in medical diagnostics and radiotherapy. Lead halide perovskites have emerged recently as a novel class of material for efficient X-ray detection. Although 3D perovskites possess very interesting optoelectronic properties they suffer from low environmental and operational stability. Here a strategy based on using starch as a polymeric template for the fabrication of stable thin film perovskite X-ray detectors is reported. The proposed p-i-n photodiodes can operate with no external bias applied (fully passive devices), reaching a top sensitivity of $5.5 \pm 0.2 \mu\text{C Gy}^{-1} \text{s}^{-1}$. The device degradation is monitored for samples stored in air for a time window of 630 days, demonstrating exceptional stability: 97% of the initial sensitivity is retained for the best perovskite-starch composite formulation making it the most stable unencapsulated perovskite X-ray detector reported so far.

1. Introduction

After cardiovascular diseases, cancer is the second deadliest disease. In 2020, 19.3 million new cancer cases were registered by the International Agency for Research on Cancer. In the same year, cancer caused 10 million death.^[1] Compared to the data from 2018, this corresponds to an increase of 6.6% in the number of new cases and a 4% increase in the number of deaths in only two years.^[2] X-rays are used in the medical field for both diagnostic and treatment of cancer patients. However, using ionizing radiation on patients can lead to undesirable effects. Indeed there is a correlation between the dose delivered in CT scans and the appearance of tumors later in life.^[3] Therefore, novel, more sensitive

and low-cost detectors for reducing and monitoring the dose delivered to the patient are crucial for the future of cancer treatments. X-rays are widely used also in scientific research to explore new materials and biological structures, in airports for security controls, and in environments with high radiation risk, such as nuclear power plants or regions where leaks of radioactive substances need to be controlled. Most of these applications would greatly benefit from the development of large-area and low-cost efficient X-ray detectors, where bulky thick wafers and single crystals show some limitations. More specifically, thin-film devices are important in space applications and portable/wearable sensors where lightness and low power consumption are crucial. Another example regards dosimeter applications, where the thin films possess low radiation absorption mimicking the X-ray energy release in human tissues. Finally, in high flux environments (e.g., synchrotron radiation, particle accelerators, nuclear reactors, and radiotherapy) thin film detectors represent a viable, radiation tolerant (thanks to low absorption), alternative to traditional detectors that quickly get damaged under strong fluences at high energies.

The leading market material for flat-panel X-ray detectors is amorphous silicon (*a*-Si).^[4] In this case, a matrix of silicon photodiodes is coupled with a scintillating material making an indirect detector. Indirect detectors suffer from low spatial resolution and are difficult to fabricate since the coupling of the scintillating material and the photodetector is not always easy.^[5,6] The most used semiconductor for direct detection in flat-panel, instead, is amorphous selenium (*a*-Se). Although superior spatial resolution


M. Verdi, A. Ciavatti, L. Basiricò, B. Fraboni
Department of Physics and Astronomy
University of Bologna
Viale Bertini Pichat 6/2, Bologna 40127, Italy
E-mail: beatrice.fraboni@unibo.it

M. Verdi, A. Ciavatti, L. Basiricò, B. Fraboni
National Institute for Nuclear Physics – INFN section of Bologna
Viale Bertini Pichat 6/2, Bologna 40127, Italy

A. Giuri, A. Rizzo
CNR NANOTEC - Istituto di Nanotecnologia
73100, c/o Campus Ecotekne, Via per MonteroniLecce, Italy

C. Esposito Corcione
Dipartimento di Ingegneria dell'Innovazione
Università del Salento
via per Monteroni, km 1, Lecce 73100, Italy

S. Colella
CNR NANOTEC – Istituto di Nanotecnologia
C/o Dipartimento di Chimica
Università di Bari
Via Orabona 4, Bari 70126, Italy
E-mail: silvia.colella@nanotec.cnr.it

 The ORCID identification number(s) for the author(s) of this article can be found under <https://doi.org/10.1002/admi.202300044>

© 2023 The Authors. Advanced Materials Interfaces published by Wiley-VCH GmbH. This is an open access article under the terms of the Creative Commons Attribution License, which permits use, distribution and reproduction in any medium, provided the original work is properly cited.

DOI: 10.1002/admi.202300044

has been demonstrated,^[7] *a*-Se has a low mobility-lifetime product ($\mu\tau$) that limits its performance at low bias, thus requiring an electric field ($80 \text{ V } \mu\text{m}^{-1}$) to operate efficiently.^[8,9] Polycrystalline cadmium zinc telluride (CZT) is an interesting alternative thanks to its high effective atomic number and good transport properties. However, like *a*-Se, CZT films are obtained through thermal deposition techniques requiring high vacuum and high temperature, thus reducing the scalability of the technology.^[10] Moreover, *a*-Si, *a*-Se, and CZT are intrinsically stiff materials and the high-temperature fabrication techniques make them incompatible with their deposition on flexible plastic substrates. Flexible and very sensitive X-ray detectors have been recently demonstrated using thin film organic semiconductors, fabricated by solution deposition over large areas.^[11–13] The disadvantages of organic semiconductors are the low absorption coefficient to X-rays and the slow time response.^[11] The first is due to the light elements inside the atomic structure since they are mainly composed of carbon and hydrogen. The slow time response ($>10 \text{ s}$) is a consequence of the photoconductive gain effect.^[14] Since 2015 hybrid lead-halide perovskites have attracted increasing attention as an interesting alternative to traditional semiconductors used for radiation detection. Hybrid Lead halide 3D perovskites have APbX_3 as chemical formula, where A is a small organic cation such as methylammonium (MA), formamidinium (FA), and X is a halide atom, typically iodine. The presence of heavy elements inside the atomic structure ensures a high X-ray absorption coefficient even at high X-rays energies. Large $\mu\tau$ values were observed even in polycrystalline films. High performance detectors were demonstrated in both polycrystalline and single crystal forms,^[15–20] and they present the great advantage of being deposited with low-cost techniques from solution on large area substrates.^[21] In fact, flexible perovskite X-ray detectors have been recently reported.^[22–24] Besides 3D, also low dimensional perovskites have been used for the fabrication of ionizing radiation detectors.^[25,26] However, medical devices require long shelf life, thus the resolution of the stability issue of 3D perovskites detectors is a strict requirement for the advancement of the field.^[27] Though, Hybrid perovskites are sensible to H_2O and O_2 ; for example MAPbI_3 , when exposed to air, reacts with moisture and decomposes to the initial PbI_2 :

Reactions with oxygen or catalyzed by UV light lead to the formation of volatile organic species such as methylamine) that can leave the perovskite film, leading to the starting lead iodine^[28,29] Since PbI_2 has a typical yellow color, a clear sign of degradation of iodine-based perovskite is the change in color from black/dark to yellow. Heat can also degrade perovskites producing volatile compounds.^[30] Ion migration inside perovskites is another mechanism that can lead to device degradation.^[31] Medical devices require long shelf life, thus the resolution of the stability issue of 3D perovskite detectors is a strict requirement for the advancement of the field.^[27] In fact, operational and environmental instability is limiting the commercialization of perovskite-based devices. Although encapsulation can limit device degradation, it is also mandatory to find a new solution to increase the intrinsic stability of perovskites.^[32]

While in the perovskite solar cell community it is already common practice to measure and track the performance degradation of devices, in the X-ray detector community researchers are only recently starting to rigorously follow the operational and environ-

mental stability of perovskite-based devices. To the best of our knowledge, the longest reported study on perovskite X-ray detectors is from Deumel et al. for encapsulated detectors that show a 20% decrease in sensitivity after 1.5 years after fabrication.^[33] Another study reports the degradation of a polycrystalline MAPbI_3 detector encapsulated in polydimethylsiloxane (PDMS) after 9 months in a glovebox.^[20]

Although device encapsulation is a viable strategy, we propose a new approach that aims at producing stable X-ray detectors through the increase of the perovskite active layer intrinsic stability. We rely on the use of a polymeric template for the growth of perovskite polycrystalline film, which confers to the film a series of characteristics that cannot be achieved with pristine perovskites, in particular higher stability in ambient conditions, improved homogeneity of the film also at greater thicknesses, and enhanced mechanical flexibility and robustness. All the above characteristics are ideal requirements for portable and flexible X-ray devices.^[34,35] The approach is highly reliable and versatile, in fact, we demonstrate it in this work for different perovskite compositions, namely MAPbI_3 and $\text{FA}_x\text{MA}_{1-x}\text{PbI}_3$. Moreover, the starch polymer allows excellent tuning of the active layer thickness, since acting as a rheological modifier enhances the viscosity of perovskite precursors' ink.^[36] We monitored over 600 days the normalized area sensitivity of thin film perovskite X-ray detectors with different active layers compositions and thicknesses implemented in a p-i-n photodiode architecture enabling the passive mode operation (0 V of external bias). It is worth noting that devices operating with no external field can further limit the perovskite degradation and increase operation stability by decreasing the ion migration. We found that a 15 wt.% starch concentration in the perovskite precursor solution, corresponding to 1050 nm thick perovskite layer provides the best trade-off between X-ray absorption, charge collection efficiency, and performance stability. We measured a sensitivity of $5.5 \pm 0.2 \mu\text{C Gy}^{-1} \text{ s}^{-1}$, comparable or even higher than other perovskite thin film detector in the literature.^[18,22,37] We report no degradation of the electric characteristic after 9.4 Gy irradiation. We found that this improved resistance of perovskite/polymer composite translates in more stable X-ray photon detectors as well, which can be stored in ambient conditions for >20 months, retaining 97% of their sensitivity.

2. Results and Discussion

We used methylammonium lead iodide (MAPbI_3 , herein MAPI) and mixed formamidinium-methylammonium lead iodide ($\text{FA}_x\text{MA}_{1-x}\text{PbI}_3$, herein FAMA) perovskite, in combination with starch to deposit, from solution, the perovskite-starch nanocomposite films (herein MAPI-xS and FAMA-xS, respectively, where in this nomenclature the x represent the concentration of starch expressed in wt.% with respect to the perovskite precursors) following the same procedure we used in our previous work,^[35] also reported in the experimental section. For both types of perovskites, we tested three different starch/precursors concentrations (10, 15, and 20 wt.%) as active layers for the X-ray photodiode. The starch concentration influences the viscosity of the starting solution to be deposited, thus it has a direct impact on the active layer thickness. A summary of all the active layers used and the respective thicknesses can be found

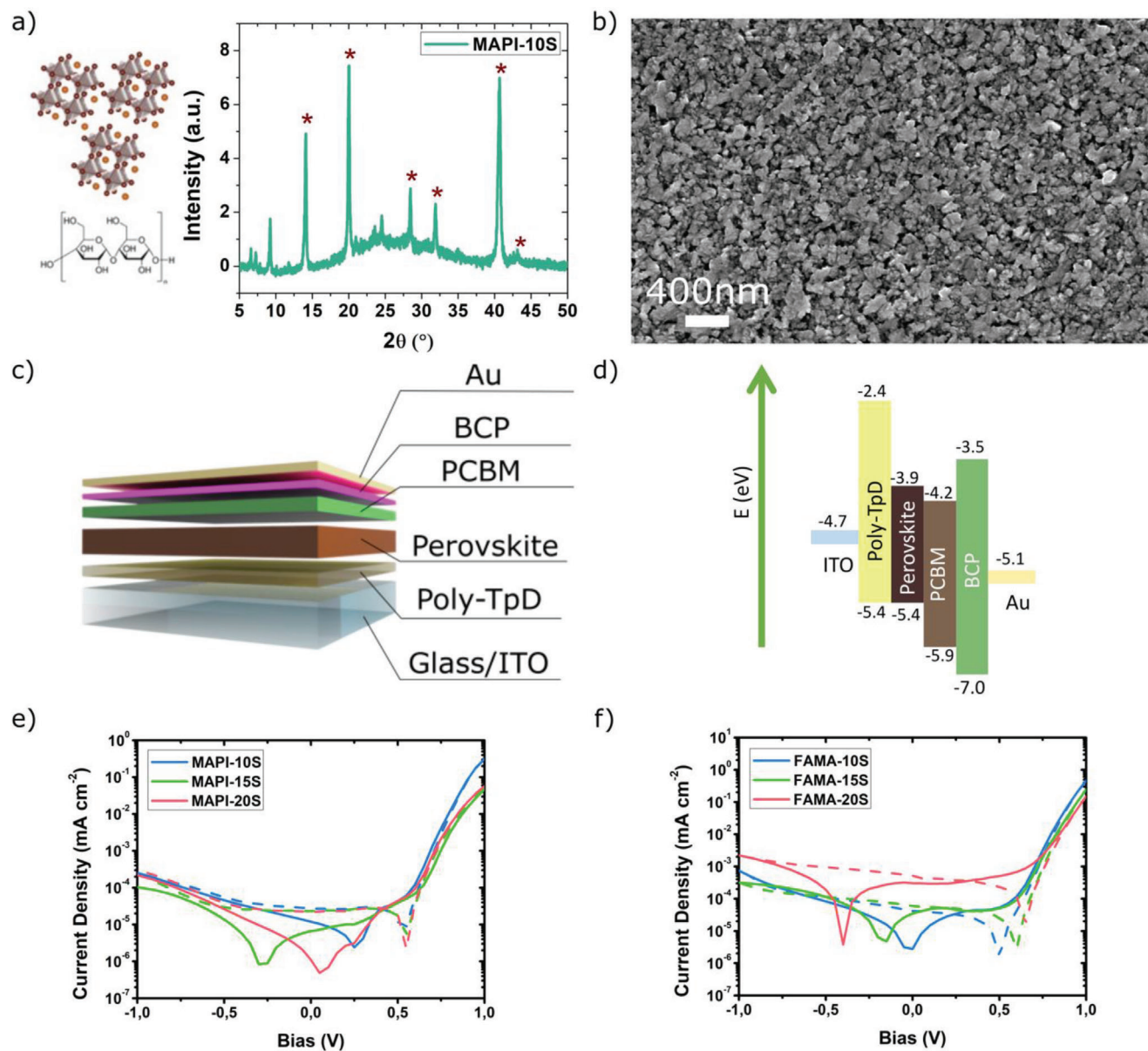


Figure 1. Perovskite-Starch nanocomposite photodiode. a) Perovskite structure (top) and starch unit chemical formula (bottom) with the XRD pattern of the nanocomposite of MAPbI_3 and starch, peaks labeled with a star are attributed to MAPbI_3 tetragonal phase. b) SEM image of the surface of the as-deposited nanocomposite thin film. c) Photodiode architecture in the p-i-n configuration fabricated on glass substrate. d) Corresponding energy levels scheme. e) Current–voltage characteristic of the MAPI-xS nanocomposites. f) Current–voltage characteristic of the FAMA-xS devices.

in Table S1 (Supporting Information) in the supporting information section. The XRD pattern of the MAPI-10S composite presents the characteristic peaks of MAPI and a very broad background attributed to the presence of the amorphous starch phase (Figure 1a). Peaks labeled with a star are attributed to the tetragonal MAPI perovskite phase, while the lower angle peaks at $2\theta = 6.55^\circ$, 7.21° , and 12.9° are attributed to an intermediate MAI- PbI_2 -DMSO complex that we always observe in a small amount when the starch is present.^[38] A SEM picture of the starch perovskite (MAPI-10S) film is reported in Figure 1b. The composite layer appears highly homogeneous and compact, completely covering the substrate. We point out that the deposition is

achieved by one step method without solvent dripping, in contrast to what is generally required to achieve a good coverage and morphology of hybrid perovskite polycrystalline films. The rheology of the precursor solutions, which strictly correlates to the starch concentration, is a key factor in the formation of perovskite films. The starch molecules form a soft and viscous matrix in which the perovskite precursors are dispersed and with which they interact via hydrogen bonding, as confirmed in our previous works.^[35,36] The starch viscous matrix acts as a template for the polycrystalline perovskite growth stemming from their self-aggregating features, eventually leading to a smooth morphology, even in thick films ($>1 \mu\text{m}$). The starch perovskite

composite is the active layer of a p-i-n configured photodiode vertical stack, fabricated on patterned ITO covered glass substrate and with the structure reported in the sketch of Figure 1c. As electron transport layer (ETL), phenyl- C_{61} -butyric acid methyl ester (PCBM) was used. For the hole transport layer (HTL), we used a layer of poly(N,N' -bis(4-butylphenyl)- N,N' -bis(phenyl)benzidine) (polyTpD), a p-type organic semiconductor employed in perovskite solar cells thanks to the favorable energy alignment between the perovskite valence band minimum and its lowest unoccupied molecular orbital (LUMO).^[39] PolyTpD is an alternative to the widely used poly(3,4-ethylenedioxythiophene) polystyrene sulfonate (PEDOT:PSS), which has proven to accelerate the degradation of the perovskite layer due to its higher hydrophilicity and ionic mobility.^[40] Moreover, the perovskite-starch HTL interface quality improves when using polyTpD instead of PEDOT:PSS resulting in better film quality.^[41] The addition of a buffer layer has been demonstrated to improve the ohmic contact with the top metal contact and, for this study we used bathocuproine (BCP).^[42] In Figure 1d, the energy level scheme of the detector structure is shown.

By simply adjusting the perovskite precursors/starch ratio, very viscous perovskite precursors inks can be obtained. This prerogative allows to fabricate thick, above 1 μm , yet homogeneous films via a single and straightforward spin-coating step. It is worth mentioning that thicker active perovskite films absorb a higher X-ray fraction, thus improving the X-ray detection capability of our devices. In this work, we fabricate devices with three different active layer thicknesses: the higher the starch concentration, the thicker the perovskite layer is. The starch concentrations used (10, 15, and 20 wt.%) resulted in 470, 1050, and 1400 nm thick active layers (Table S1, Supporting Information). We electrically characterize the photodiodes by measuring current–voltage scans (IV). The IVs measured for the two perovskites nanocomposite and three thicknesses are reported in Figure 1e,f. Higher starch concentrations lead to a decrease of the forward current in both MAPI and FAMA composites. On the contrary, FAMA-20S presents a reverse current 1 order of magnitude higher than FAMA-10S, while in the MAPI case the addition of starch does not strongly influence the reverse current. The rectification factor, calculated as the ratio between the forward current at 1 V and the reverse current at -1 V, is reported in Table S1 (Supporting Information). For all the diode structures the rectification factor is at least above 10^2 (best $>10^3$) assessing the good photodiode fabrication quality. As reference for our investigation, we fabricated and characterized a simple MAPI device, deposited with classical dripping technique as reported in materials and methods, whose characterization is reported in Figure S2 (Supporting Information) and measured in the same ambient conditions as the composite samples object of our study. The I - V characteristics (Figure S2a, Supporting Information) has very small rectification factor and further degrade after X-ray irradiation.

We tested the X-ray detection performances of the starch perovskite-based p-i-n photodiodes by measuring their current response under 40 kVp X-rays (W-target tube), **Figure 2**. The employed photodiode architecture works in fully passive mode (bias = 0 V). Indeed, the use of different materials in the multilayer structure gives rise to a heterojunction with a built-in potential. When electron-hole pairs are generated inside the per-

ovskite by the impinging X-ray photons, they are separated and driven toward the electrodes by the internal electric field with no need of external bias. The typical dynamic response of perovskite-starch films under different incident dose rates, ranging from 255 to 1333 $\mu\text{Gy s}^{-1}$, is shown in figure 2a, for a 10 s modulation period of the X-ray beam. Notably, this very stable behavior with different doses is peculiar of starch-containing active layers, indeed the reference bare MAPI shows unstable dark current even at 0 V with visible drift over time and considerable shift after each exposure as well, as reported in Figure S2b (Supporting Information). For FAMA-15s, the linear response of the photocurrent ΔI ($\Delta I = I_{\text{dark}} - I_{\text{XR}}$ where I_{dark} is the dark current and I_{XR} is the measured current when the detector is exposed to X-rays) as a function of the dose rate and the respective linear fit are reported as blue dots and red dashed line in Figure 2b. The angular coefficient of the linear fit of the photocurrent represents the sensitivity of the detector to the X-rays. All the other tested configurations have similar dynamic and linear behavior as the FAMA-15S reported in Figure 2a,b. In Figure 2c are reported the values of sensitivity divided per the detector area for the two different perovskite compositions and for all the thicknesses at bias = 0 V. Even if the attenuated fraction of FAMA is comparable to the one of MAPI (see Figure S2, Supporting Information), FAMA based photodiodes present sensitivity values $\approx 60\%$ higher than their MAPI counterpart. This agrees with previous literature results that showed improved optoelectronic performances in mixed cations perovskites, both as radiation detectors^[17,18] and solar cells.^[43–45] For both MAPI and FAMA the highest performance in terms of sensitivity was achieved when mixed with 15 wt.% of starch, likely due to an optimum balance between thickness, thus X-ray absorption cross section, and mobility of charges through the film. The top sensitivity value (in passive mode) is $5.5 \pm 0.2 \mu\text{C Gy}^{-1} \text{ s}^{-1}$ for FAMA-15S and $3.64 \pm 0.12 \mu\text{C Gy}^{-1} \text{ s}^{-1}$ for MAPI-15S. These values are comparable to the state of the art passive thin film perovskite X-ray detector with similar thicknesses.^[18,22] The relation between starch content and X-ray sensitivity can be ascribed to the different film thickness, as when dealing with ionizing radiations, higher layer thickness means higher interaction cross section. However, once the photons are converted into mobile electric charges, they have to be transported and collected to generate a detectable electric signal: a thick layer may hinder a complete collection of the generated carriers as the internal electric field is weaker and recombination processes take place. Among the thicknesses we studied, the optimum trade-off between X-ray absorption and charge collection efficiency occurs for 1050 nm thick active layers for both types of perovskites.

If a reverse bias is applied to the photodiode, an additional external electric field is acting on the active layer. Figure 2d,e reports the normalized sensitivities as a function of the reverse bias for MAPI-xS and FAMA-xS. In the case of MAPI-10S and MAPI-15S detectors, the sensitivity does not scale with bias, likely because for these thicknesses the internal electric field is already strong enough to collect all the free charges created by the incoming radiation. This hypothesis is supported by the excellent quantum efficiency of perovskite solar cells of comparable geometry, reaching almost 100% if the perovskite film and interfaces are of good quality.^[46–48] In MAPI-20S detectors (1400 nm thick), the sensitivity increases with reverse bias up to -0.6 V. Further reverse bias

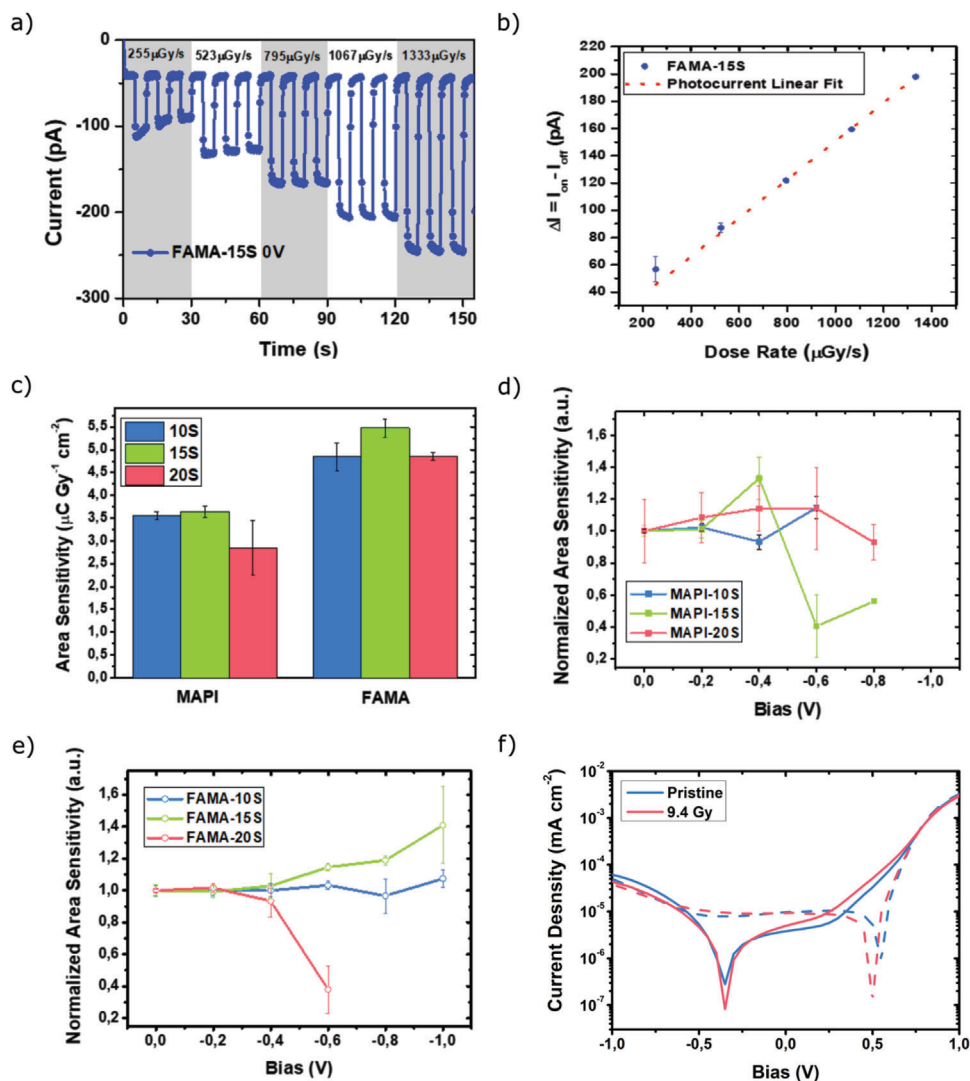


Figure 2. X-ray direct response. a) Example of the dynamic response of the perovskite-starch based X-ray detector when exposed to 40 kVp X-ray radiation with increasing dose rates and external bias set to 0 V (passive mode). The grey boxes help distinguish the different incident dose rates ranging from 255 to 1333 $\mu\text{Gy s}^{-1}$. b) The graph shows the linear behavior of the photocurrent (ΔI) as a function of the incident dose rate. c) Summary of the sensitivity per unit area for the different perovskite-starch nanocomposite X-ray detectors. d,e) Normalized sensitivity with the increase of reverse bias for the MAPI-xS and for FAMA-xS, respectively. f) I–V characteristic of MAPI-10S acquired in dark conditions before X-ray exposure (blue line) and after a cumulative dose of 9.4 Gy (red line).

increases lead to a decrease in performances, due to an increase of the dark current and a reduction of the signal to noise ratio, see Figure S4 (Supporting Information). Looking at the bias dependence of the sensitivity for FAMA based devices, FAMA-10S (470 nm) present no relevant effects while FAMA-15S (1050 nm film) based devices show a slight sensitivity increase with reverse bias, reaching the highest value of $7.8 \pm 1.2 \mu\text{C Gy}^{-1} \text{cm}^{-2}$ at -1 V . The effect of reverse bias on both FAMA-20S and MAPI-20S devices is to decrease the performances. We ascribe this observation to the presence of high starch concentration in the precursor solution, possibly leading to the formation of phase segregation and localized higher conductive paths thus decreasing the shunt resistance for both MAPI-20S and FAMA-20S films. The small increase of X-ray photocurrent due to extra charges generated and collected inside the active layer results to be a minor effect with

respect to the increase of dark current, thus leading to lower sensitivities.

Because of ion migration, bias related stability is a known issue in perovskite-based devices.^[49] Dark current stability is crucial for high performance ionizing radiation detection. Therefore, it is noteworthy that the here proposed thin film p-i-n photodiode architecture ensures a good charge collection efficiency at very low external bias or even at 0 V applied (passive mode). Operation in passive mode offers a great advantage for operational stability. Indeed, if a bias is applied, even a small one, a drift in the dark current appears. In Figure S5 (Supporting Information) are reported for MAPI-10S the current response under repeated X-ray on/off cycles for >10 min with 5 s pulse and 50% duty cycle, in passive mode (Figure S5a, Supporting Information) and with 0.5 V of reverse bias (Figure S5b, Supporting Information). Data acquired

with the reverse bias applied show the presence of a strong drift in the dark current. When operating in passive mode the detector shows a remarkably stable and repeatable response without any drift.

Another important figure of merit for ionizing radiation detectors is the limit of detection (LoD), defined as the incident dose rate value at which the photocurrent is three times the RMS value of the dark current.^[50] The measured LoD at 0 V for MAPI-xS and FAMA-xS are shown in Figure S6 (Supporting Information). The best LoD was found for MAPI-10S and is $7.3 \pm 0.4 \mu\text{Gy s}^{-1}$, a value comparable to the typical dose rates used in medical diagnostic applications (typically $>5.5 \mu\text{Gy s}^{-1}$)^[51] and lower of some values reported in literature for thin film perovskites.^[23,52] Noteworthy, the thinnest active layer exhibited the best LoD, as a demonstration of the high material quality.

Figure 2f reports the current–voltage (*I*–*V*) characteristic for a MAPI-10S device measured in the dark before and after exposure to 9.6 Gy of 40 kVp X-rays, a large dose, corresponding to thousands of X-ray images with standard medical diagnostic X-ray apparatuses. No sign of degradation is visible in the electrical characteristics, with almost identical reverse and forward current values. Therefore, we assessed the high radiation tolerance of the detectors under study, another advantage of thin-film technology for ionizing radiation detection, especially when compared to other bulky perovskite detectors.^[53]

Stability in air and aging effects are among the crucial aspects of thin film perovskite devices. The addition of starch strongly improved the stability in air of solar cells.^[35] To assess aging effects and the device stability over long periods of time, we stored the samples in the ambient atmosphere and in the dark. The temperature and relative humidity variation in 1 year can be found in Figure S7 (Supporting Information) that could possibly affect the device response. We measured the sensitivity of the devices to 40 kVp X-rays for over one and a half years from the fabrication day, considered the day 0. It is worth noticing that most of reference MAPI devices fully degrade shortly after the first characterization at time zero, therefore it was not possible to perform any statistically significant aging test. Only one device out of nine fabricated showed a measurable signal after 100 h with halved sensitivity with respect to time 0. Starch-based devices, on the other hand, showed a quite reproducible behavior for all measured samples. **Figure 3a,b** shows the average sensitivity for MAPI-xS and FAMA-xS devices. At day 0, FAMA based nanocomposites have higher sensitivities but they degrade faster than MAPI based ones. The degradation is more pronounced for FAMA-20S devices, where a drop of 72% in performance occurs after 138 days. Instead, in MAPI based nanocomposite the decrease in performance is only 23% after 138 days for MAPI-10S, while for MAPI-20S the point at 0 and 138 days are comparable within the error bar. After 630 days of storage, FAMA-20S sensitivity decreases down to $1.36 \pm 0.02 \mu\text{C Gy}^{-1} \text{s}^{-1}$ ($>70\%$), MAPI-10S show a 34% sensitivity decrease, while for MAPI-20S the percentage decrease is only 7%. **Figure 3c** shows the X-ray photocurrent response after 630 days of storage with 0 V bias: the response is highly reproducible, regardless of the type of composite.

The better stability of MAPI nanocomposites compared to FAMA based ones is evident. MAPI-10S and MAPI-20S have comparable photocurrent values, while FAMA-10S has a higher response than FAMA-20S. It is well known that 3D iodine-based

hybrid perovskite becomes yellow after exposure to air due to the formation of lead iodide PbI_2 that has a yellow color.^[29,54–56] Recently, A. Alberti and co-workers reported TEM studies of MAPI perovskite degradation, suggesting 2H polymorphism of PbI_2 as the main cause of degradation.^[57] All our films show a dark color with no visible sign yellow phase, **Figure 3d**, even after exposure to air for 630 days.

Given the recent extraordinary performance improvements reported for perovskite X-ray and gamma detectors, their application in real-life environments is soon to be expected and this requires an assessment of their long-term performance and stability. While in the perovskite solar cell community monitoring time stability is an established practice,^[58] this is not the case for perovskite radiation detectors: among all the papers published in the last years on this topic, only a few of them report on the device stability under operation^[17,26,59–63] and even fewer about aging effects.^[17,20,26,61,64–66] The few reports on aging measurement on 3D perovskite polycrystalline detectors deal with encapsulated detectors. The present work reports, for the first time, a long-term monitoring of aging effects for not-encapsulated perovskite thin film radiation detectors. We have been able to assess how the most stable devices (MAPI-20S) retain 97% of their sensitivity after 630 days of storage in air, a significantly longer period than any other report in the literature for unencapsulated devices and surpasses the longest aging test (630 days) for an encapsulated devices.

Figure 4a shows the relative sensitivity variation for MAPI-10S and FAMA-10S, with identical active layer thickness. The slower degradation of MAPI-10S compared to FAMA-10S is evident. In our previous publication on the effect of starch addition to perovskite solution for solar cells,^[35] we observed an improved solar cell performance stability in the case of perovskite-starch composite. It is worth mentioning that for this study we used gold as top metallic contact instead of aluminum. **Figure 4b** shows the *I*–*V* characteristics, under 1 sun illumination, between the devices after fabrication and after 630 days of storage. In pristine conditions MAPI-20S shows the lowest power conversion efficiency (PCE) consistent with the lowest X-ray sensitivity observed, see **Table S8** (Supporting Information).

It is noteworthy that MAPI-10S shows a decrease in PCE of $>70\%$ while the decrease in X-ray sensitivity is 34%, as mentioned before. We speculate that the difference in degradation arises from the different photon energy involved. When a visible photon reaches the perovskite layer, it gets absorbed at a specific depth of the active layer and the device has to separate the exciton and transport the photogenerated charges to the respective collecting electrodes across the interlayers. On the contrary, X-rays generate charges over the whole perovskite layer volume and since the energy involved is much higher the exciton does not form. Therefore, the process of generation, transport and collection of photoinduced charges is much more efficient following X-ray exposure.

3. Conclusion

In this study, we demonstrate the use of starch as a polymeric template for the fabrication of ambient stable thin film perovskite X-ray detectors. Besides conferring to the perovskite film superior properties, the starch addition in the precursor solutions also

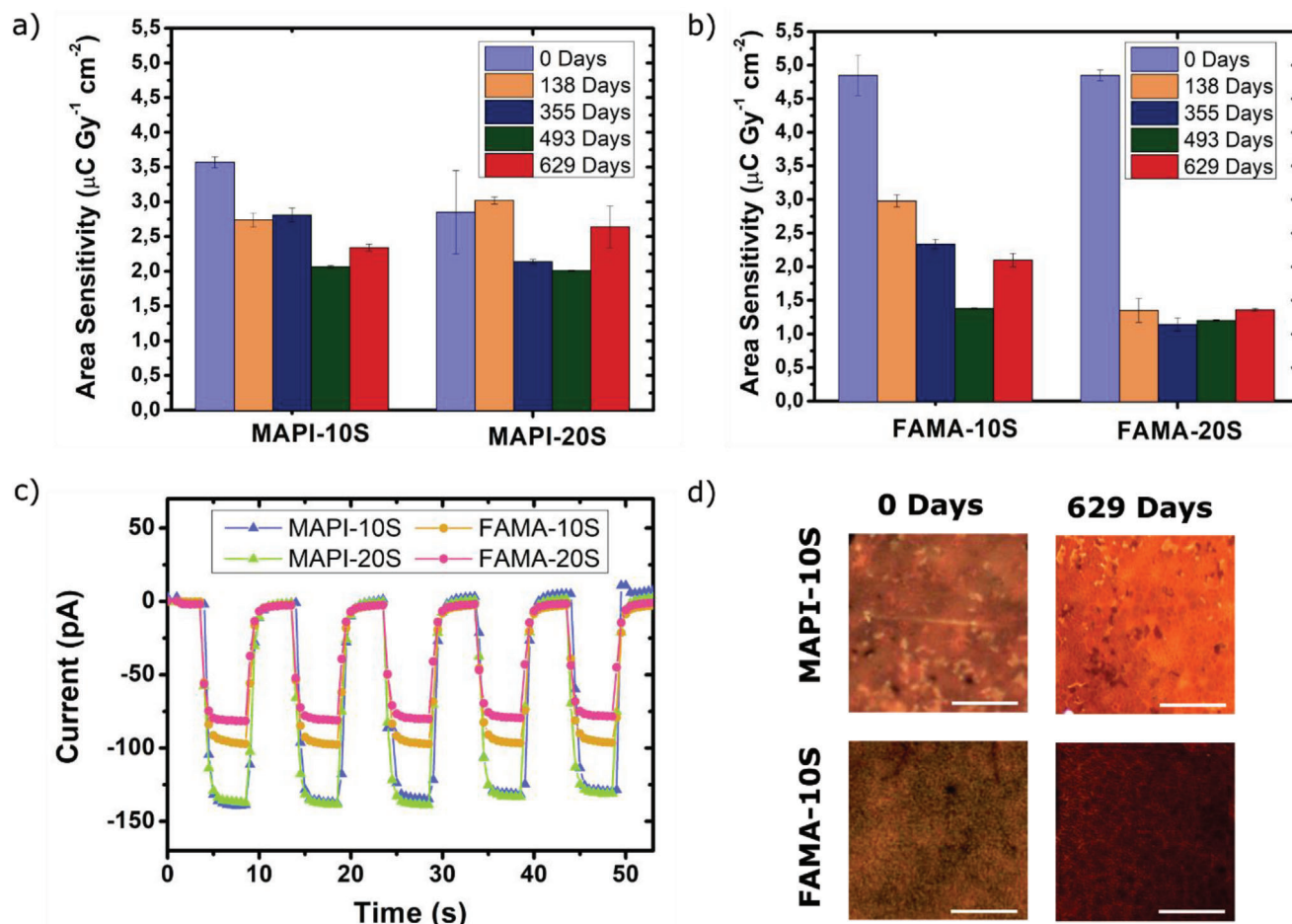


Figure 3. Aging and device stability a,b) Aging bar charts of the area sensitivity for MAPI- and FAMA-starch nanocomposite respectively. The sensitivity values are averaged over four devices and the error bars represent the statistical deviation. In the graphs are reported the sensitivity values for MAPI-10S, MAPI-20S, FAMA-10S, and FAMA-20S up to 630 days. All the devices were kept in air and in dark storage condition. c) Photocurrent response under 40 kVp X-ray for MAPI-10S, MAPI-20S, FAMA-10S, and FAMA-20S acquired after 630 days of storage in air at 0 V, incident dose rate of 1334 μGy s⁻¹. d) Comparison of the optical pictures of MAPI-10S and FAMA-10S taken at the day 0 and the pictures taken after 630 days of storage, the scale bar is 500 μm.

allowed to achieve an excellent control over the perovskite film thickness. We studied 3 different thicknesses finding the best trade-off between X-ray absorption, charge collection efficiency and detector performance to be 1050 nm for MAPI and FAMA. p-i-n photodiodes with FAMA-15S were found to be the best performing devices with a top sensitivity of $5.5 \pm 0.2 \mu\text{C Gy}^{-1} \text{s}^{-1}$ at 0 V external bias. The photodiode architecture gives the possibility to work in passive mode. With no external bias, ion migration is limited, increasing the operational stability of the detectors. We studied sensitivity as a function of the external bias, finding no significant improvement in the performances. Therefore, we propose the fully passive mode operation as the most effective one. The lowest limit of detection was found for 450 nm thick MAPI-10S to be $7.3 \pm 0.4 \mu\text{Gy s}^{-1}$, lower than others reported in the literature for thin film perovskite X-ray detectors. We observed no degradation in the electrical characteristic after 9.4 Gy exposure. To verify the stability of the proposed unencapsulated detectors, we stored them in air for 630 days. The samples were subjected to temperatures and relative humidity as high as 30 °C

and 70% respectively during summer times. After 1.7 years the films retained their dark color and nice dynamics curves under 40 kVp X-rays were measured. We monitored the degradation of the detectors by measuring the sensitivity over 630 days making this work the longest study on perovskite X-ray detectors aging. We found FAMA-xS based devices degraded more than MAPI-xS ones. MAPI-20S retained 97% of the initial area sensitivity after the storage, thus resulting in the most stable unencapsulated direct perovskite X-ray detector proven so far. Therefore, we propose the starch polymeric template as an effective method to improve perovskite X-ray detectors stability avoiding the need for encapsulation.

4. Experimental Section

Sample Fabrication: The perovskite precursor solutions were prepared in a N₂-filled glovebox, starting from an equimolar stoichiometric ratio (1:1) of CH₃NH₃ and PbI₂ in DMSO with a precursor concentration of

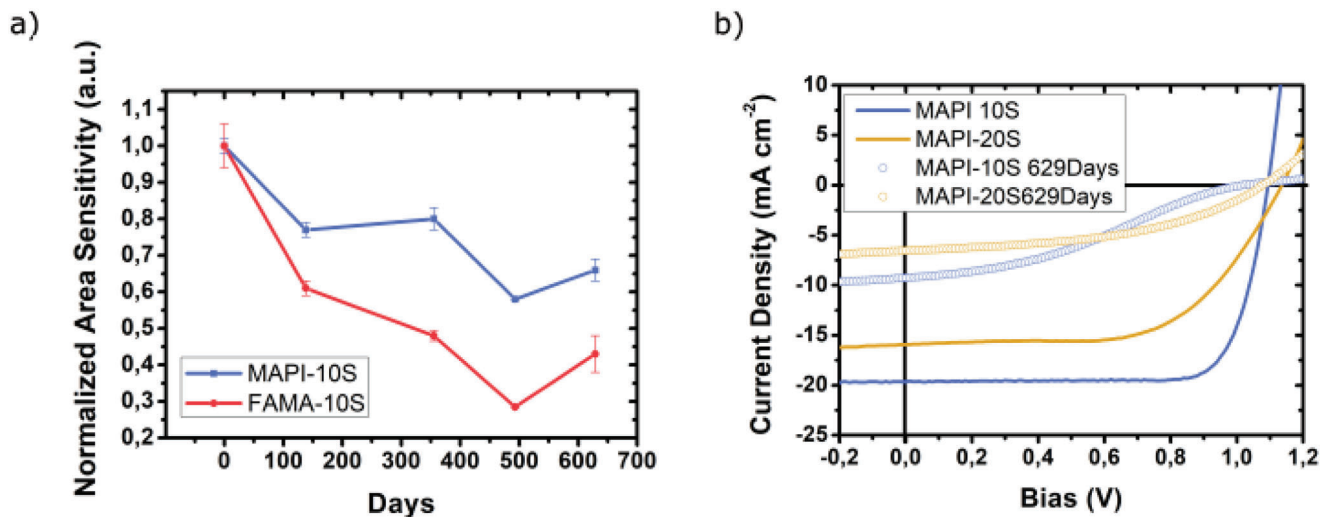


Figure 4. X-ray detector and Solar cell aging. A) Relative variation of X-ray sensitivity for MAPI-10S, FAMA-10S active layer. The layer thickness in the two cases was 470 nm. B) I–V characteristics under 1 sun illumination of pristine MAPI-starch composite-based devices and I–V characteristics after 630 days of storage in air and dark showing a big change in V_{oc} for the device without the starch composite.

30 wt.%. The solutions were stirred at 80 °C for 30 min. Starch (Maize, Aldrich) was added to the as prepared perovskite precursor's solution in different percentage (i.e., 0, 10, 15, 20 wt.%) then the solutions were stirred further at 80 °C for 5 h.

For the reference MAPI without starch in the formulation, a 48 wt.% solution of N,N-dimethylformamide anhydrous (DMF, 99.8%, Sigma–Aldrich, St. Louis, MO, USA), containing 1:1:1 mol of Methylammonium iodide (MAI, Greatcellsolar, Queanbeyan, Australia), PbI₂ (Alfa Aesar), and anhydrous dimethyl sulfoxide (DMSO, 99.9%, Sigma–Aldrich) was prepared.

For device fabrication, pre-patterned ITO coated substrates were sequentially cleaned by ultrasonication in acetone and deionized water. After plasma treatment, a solution of poly-TPD (1.5 mg ml⁻¹ in CB) was deposited on glass/ITO by spin-coating at 4000 rpm for 60 s. The films were annealed at 110 °C for 30 min in air followed by UV treatment in air for 30 min to improve the poly-TPD wettability. The as prepared substrates were transferred in the N₂-filled glovebox where perovskite starch-films were prepared by spin-coating at 9000 rpm for 20 s on the poly-TPD film, followed by annealing at 100 °C for 30 min. Reference MAPI films, instead, were prepared by spin-coating onto the treated substrates at 4000 rpm for 25 s with a dripping of anhydrous toluene (99.8%, Sigma–Aldrich) at 15 s before the end of the spinning. The obtained films were subsequently annealed onto a hot plate (100 °C, for 10 min) and then cooled to room temperature.

Finally, PCBM (25 448 mg mL⁻¹ in CB) and BCP (0.5 mg mL⁻¹ in IPA) solutions were sequentially deposited at 1000 rpm for 60 s and at 5000 rpm for 20 s, respectively to complete the device stack. Au cathodes were evaporated through a shadow mask in a high vacuum. The active area of the devices was 0.04 cm². For the reference device, the perovskite–starch film was replaced by a standard MAPbI₃ perovskite, following a previously published procedure.^[67] Briefly, precursors' solutions were prepared by dissolving stoichiometric amounts of MAI, PbI₂, and DMSO (1:1:1) in dimethylformamide with a concentration of 48 wt.%. The films were prepared by spin-coating at 4000 rpm for 25 s, and the toluene was dripped onto the substrate after 15 s from the beginning of the process. The coated substrates were annealed at 100 °C for 10 min on a hot plate.

X-Ray Characterization: Electrical characterization of the samples under X-ray irradiation was performed in a faraday box with a 70 μm front Al window. The X-ray source used was a Hamamatsu L12161 X-ray tube with a tungsten target with a fixed 40 kV operating voltage. The filament current was changed between 100 and 500 μA leading to an incident dose

rate on the samples (38 cm from source) between 318 and 1665 μGy s⁻¹. The X-ray tube used in this work was periodically (every 6 months) calibrated with a commercial dosimeter Barracuda-RT1, with silicon dosimeter probe, with certified calibration. The calibration procedure was performed by placing the barracuda dosimeter at the same distance and on the same sample holder of the devices under test and mediating the dose rate over ten consecutive irradiations of 10 s each. The modulation of the beam was obtained with a mechanical lead shutter placed close to the X-ray tube window. A Keithley SMU 2614 was used for current signal acquisition. For the aging tests the devices were kept (in dark inside a plastic box, in air, and wrapped in aluminum foil).

Solar Cell Characterization: Current–voltage characteristics of the solar cells were measured by using a Keithley 2400 Source Measure 473 Unit and an Air Mass 1.5 Global (AM1.5G) solar simulator (Newport 474 91160A) under an irradiation intensity of 100 mW cm⁻². The measurement was made setting a range of voltage from 1.2 to –0.2476 V in the reverse mode.

Scanning Electron Microscopy: Morphological characterization was performed by ZEISS Sigma Field Emission Scanning Electron Microscope instrument in high vacuum and high-resolution mode, equipped with Gemini column and an integrated high efficiency in-lens detector. A 5 kV voltage acceleration was applied.

X-Ray Diffraction Measurements: X-ray diffraction was collected using an X-ray diffractometer (D8 Advance, Bruker AXS) (Cu K α , wavelength of $\lambda = 1.5406 \text{ \AA}$) within the range of 5–50°.

Supporting Information

Supporting Information is available from the Wiley Online Library or from the author.

Conflict of Interest

The authors declare no conflict of interest.

Author Contributions

M.V. and A.C. characterized the photodiodes electrically and under X-rays. A.G. fabricated the samples and performed SEM, XRD and characterized

the samples under solar simulator. M.V. prepared the manuscript. A.R. and L.B. contributed to data analysis and interpretation of the results. S.C. and B.F. coordinated the whole project. All the authors contributed in manuscript preparation. All the authors participated in scientific discussion and revision of the manuscript.

Data Availability Statement

The data that support the findings of this study are available from the corresponding author upon reasonable request.

Keywords

aging, perovskite, stability, X-ray detectors

Received: February 7, 2023

Revised: April 21, 2023

Published online: May 28, 2023

- [1] H. Sung, J. Ferlay, R. L. Siegel, M. Laversanne, I. Soerjomataram, A. Jemal, F. Bray, *CA A Cancer J. Clin.* **2021**, *71*, 209.
- [2] F. Bray, J. Ferlay, I. Soerjomataram, R. L. Siegel, L. A. Torre, A. Jemal, *Ca-Cancer J. Clin.* **2018**, *68*, 394.
- [3] E. C. Lin, *Mayo. Clin. Proc.* **2010**, *85*, 1142.
- [4] X-ray flat panel detectors market size, share and industry analysis by product type, *Fortune, Healthcare Market Research Report*, **2019**, p. 160.
- [5] H. G. Chotas, J. T. Dobbins, C. E. Ravin, *Radiology* **1999**, *210*, 595
- [6] G. F. Knoll, *Radiation Detection and Measurement*, 4th ed., John Wiley, Hoboken N.J. **2010**
- [7] G. Hajdok, J. J. Battista, I. A. Cunningham, *Med. Phys.* **2008**, *35*, 3180.
- [8] H. Huang, S. Abbaszadeh, *IEEE Sens. J.* **2020**, *20*, 1694.
- [9] S. Kasap, J. B. Frey, G. Belev, O. Tounignant, H. Mani, L. Laperriere, A. Reznik, J. A. Rowlands, *Phys. Status Solidi B* **2009**, *246*, 1794.
- [10] X. Gao, H. Sun, D. Yang, P. Wangyang, C. Zhang, X. Zhu, *Vacuum* **2021**, *183*, 109855.
- [11] A. Ciavatti, L. Basiricò, I. Fratelli, S. Lai, P. Cosseddu, A. Bonfiglio, J. E. Anthony, B. Fraboni, *Adv. Funct. Mater.* **2019**, *29*, 1806119.
- [12] I. Temiño, L. Basiricò, I. Fratelli, A. Tamayo, A. Ciavatti, M. Mas-Torrent, B. Fraboni, *Nat. Commun.* **2020**, *11*, 2136.
- [13] A. Tamayo, I. Fratelli, A. Ciavatti, C. Martínez-Domingo, P. Branchini, E. Colantoni, S. De Rosa, L. Tortora, A. Contillo, R. Santiago, S. T. Bromley, B. Fraboni, M. Mas-Torrent, L. Basiricò, *Adv. Electron. Mater.* **2022**, *8*, 2200293.
- [14] L. Basiricò, A. Ciavatti, T. Cramer, P. Cosseddu, A. Bonfiglio, B. Fraboni, *Nat. Commun.* **2016**, *7*, 13063.
- [15] H. Wei, D. DeSantis, W. Wei, Y. Deng, D. Guo, T. J. Savenije, L. Cao, J. Huang, *Nat. Mater.* **2017**, *16*, 826.
- [16] H. Wei, Y. Fang, P. Mulligan, W. Chuirazzi, H.-H. Fang, C. Wang, B. R. Ecker, Y. Gao, M. A. Loi, L. Cao, J. Huang, *Nat. Photonics* **2016**, *10*, 333.
- [17] Y. Liu, Y. Zhang, X. Zhu, J. Feng, I. Spanopoulos, W. Ke, Y. He, X. Ren, Z. Yang, F. Xiao, K. Zhao, M. Kanatzidis, S. (Frank) Liu, *Adv. Mater.* **2021**, *33*, 2006010.
- [18] L. Basiricò, S. P. Senanayak, A. Ciavatti, M. Abdi-Jalebi, B. Fraboni, H. Siringhaus, *Adv. Funct. Mater.* **2019**, *29*, 1902346.
- [19] S. Yakunin, M. Sytnyk, D. Krieger, S. Shrestha, M. Richter, G. J. Matt, H. Azimi, C. J. Brabec, J. Stangl, M. V. Kovalenko, W. Heiss, *Nat. Photonics* **2015**, *9*, 444.
- [20] A. Glushkova, P. Andričević, R. Smajda, B. Náfrádi, M. Kollár, V. Djokić, A. Arakcheeva, L. Forró, R. Pugin, E. Horváth, *ACS Nano* **2021**, *15*, 4077.
- [21] L. Basiricò, A. Ciavatti, B. Fraboni, *Adv. Mater. Technol.* **2021**, *6*, 2000475.
- [22] S. Demchyshyn, M. Verdi, L. Basiricò, A. Ciavatti, B. Hailegnaw, D. Cavalcoli, M. C. Scharber, N. S. Sariciftci, M. Kaltenbrunner, B. Fraboni, *Adv. Sci.* **2020**, *7*, 2002586.
- [23] H. Mescher, F. Schackmar, H. Eggers, T. Abzieher, M. Zuber, E. Hamann, T. Baumbach, B. S. Richards, G. Hernandez-Sosa, U. W. Paetzold, U. Lemmer, *ACS Appl. Mater. Interfaces* **2020**, *12*, 15774.
- [24] A. Ciavatti, R. Sorrentino, L. Basiricò, B. Passarella, M. Caironi, A. Petrozza, B. Fraboni, *Adv. Funct. Mater.* **2021**, *31*, 2009072.
- [25] F. Lédée, A. Ciavatti, M. Verdi, L. Basiricò, B. Fraboni, *Adv. Opt. Mater.* **2022**, *10*, 2101145.
- [26] H. Li, J. Song, W. Pan, D. Xu, W. Zhu, H. Wei, B. Yang, *Adv. Mater.* **2020**, *32*, 2003790.
- [27] N. Chandrashekar, S. M. Gautam, K. S. Srinivas, J. Vijayananda, in *Fourth International Conference on Software Engineering Research, Management and Applications (SERA'06)*, IEEE, Seattle, WA, USA **2006**, pp. 5–12.
- [28] G. Niu, X. Guo, L. Wang, *J. Mater. Chem. A* **2015**, *3*, 8970.
- [29] C. C. Boyd, R. Cheacharoen, T. Leijtens, M. D. McGehee, *Chem. Rev.* **2019**, *119*, 3418.
- [30] L. Shi, M. P. Bucknall, T. L. Young, M. Zhang, L. Hu, J. Bing, D. S. Lee, J. Kim, T. Wu, N. Takamura, D. R. McKenzie, S. Huang, M. A. Green, A. W. Y. Ho-Baillie, *Science* **2020**, *368*, eaba2412.
- [31] T. Zhang, C. Hu, S. Yang, *Small Methods* **2020**, *4*, 1900552.
- [32] Q. Fu, X. Tang, B. Huang, T. Hu, L. Tan, L. Chen, Y. Chen, *Adv. Sci.* **2018**, *5*, 1700387.
- [33] S. Deumel, A. J. J. M. van Breemen, B. Peeters, J. Maas, H. B. Akkerman, E. A. Meulenlamp, G. H. Gelinck, J. E. Huerdler, O. Schmidt, W. Heiss, S. F. Tedde, In *Medical Imaging 2022: Physics of Medical Imaging* (Eds: W. Zhao, L. Yu), SPIE, San Diego, United States **2022**, 8.
- [34] A. Giuri, N. Rolston, S. Colella, A. Listorti, C. Esposito Corcione, H. Elmaraghi, S. Lauciello, R. H. Dauskardt, A. Rizzo, *ACS Appl. Energy Mater.* **2021**, *4*, 11194.
- [35] A. Giuri, S. Masi, A. Listorti, G. Gigli, S. Colella, C. Esposito Corcione, A. Rizzo, *Nano Energy* **2018**, *54*, 400.
- [36] A. Giuri, R. Munir, A. Listorti, C. Esposito Corcione, G. Gigli, A. Rizzo, A. Amassian, S. Colella, *Nanotechnology* **2021**, *32*, 265707.
- [37] H. S. Gill, B. Elshahat, A. Kokil, L. Li, R. Mosurkal, P. Zymanski, E. Sajo, J. Kumar, *Phys. Med.* **2018**, *5*, 20.
- [38] N. J. Jeon, J. H. Noh, Y. C. Kim, W. S. Yang, S. Ryu, S. I. Seok, *Nat. Mater.* **2014**, *13*, 897.
- [39] O. Malinkiewicz, A. Yella, Y. H. Lee, G. M. Espallargas, M. Graetzel, M. K. Nazeeruddin, H. J. Bolink, *Nat. Photonics* **2014**, *8*, 128.
- [40] H. Chen, Y. Hou, C. E. Halbig, S. Chen, H. Zhang, N. Li, F. Guo, X. Tang, N. Gasparini, I. Levchuk, S. Kahmann, C. O. Ramirez Quiroz, A. Osvet, S. Eigler, C. J. Brabec, *J. Mater. Chem. A* **2016**, *4*, 11604.
- [41] Z. Safari, M. B. Zarandi, A. Giuri, F. Bisconti, S. Carallo, A. Listorti, C. Esposito Corcione, M. R. Nateghi, A. Rizzo, S. Colella, *Nanomaterials* **2019**, *9*, 1627.
- [42] C. Chen, S. Zhang, S. Wu, W. Zhang, H. Zhu, Z. Xiong, Y. Zhang, W. Chen, *RSC Adv.* **2017**, *7*, 35819.
- [43] N. J. Jeon, J. H. Noh, W. S. Yang, Y. C. Kim, S. Ryu, J. Seo, S. I. Seok, *Nature* **2015**, *517*, 476.
- [44] M. Lyu, N.-G. Park, *Sol. RRL* **2020**, *4*, 2000331.
- [45] N. Pellet, P. Gao, G. Gregori, T.-Y. Yang, M. K. Nazeeruddin, J. Maier, M. Grätzel, *Angew. Chem., Int. Ed.* **2014**, *53*, 3151.
- [46] M. M. Lee, J. Teuscher, T. Miyasaka, T. N. Murakami, H. J. Snaith, *Science* **2012**, *338*, 643.

- [47] A. Riquelme, F. E. Gálvez, L. Contreras-Bernal, H. Míguez, J. A. Anta, *J. Appl. Phys.* **2020**, *128*, 133103.
- [48] B. Yang, O. Dyck, J. Poplawsky, J. Keum, A. Puzos, S. Das, I. Ivanov, C. Rouleau, G. Duscher, D. Geohegan, K. Xiao, *J. Am. Chem. Soc.* **2015**, *137*, 9210.
- [49] Y. Yuan, J. Huang, *Acc. Chem. Res.* **2016**, *49*, 286.
- [50] *Spectrochim Acta Part B At Spectrosc* **1978**, *33*, 241.
- [51] I. Clairand, J.-M. Bordy, E. Carinou, J. Daures, J. Debroas, M. Denozière, L. Donadille, M. Ginjaume, C. Itié, C. Koukorava, S. Krim, A.-L. Lebacqz, P. Martin, L. Struelens, M. Sans-Merce, F. Vanhavere, *Radiat. Meas.* **2011**, *46*, 1252.
- [52] J. Liu, B. Shabbir, C. Wang, T. Wan, Q. Ou, P. Yu, A. Tadich, X. Jiao, D. Chu, D. Qi, D. Li, R. Kan, Y. Huang, Y. Dong, J. Jasieniak, Y. Zhang, Q. Bao, *Adv. Mater.* **2019**, *31*, 1970214.
- [53] G. Armaroli, L. Ferlauto, F. Lédée, M. Lini, A. Ciavatti, A. Kovtun, F. Borgatti, G. Calabrese, S. Milita, B. Fraboni, D. Cavalcoli, *ACS Appl. Mater. Interfaces* **2021**, *13*, 58301.
- [54] J. M. Frost, K. T. Butler, F. Brivio, C. H. Hendon, M. van Schilfgarde, A. Walsh, *Nano Lett.* **2014**, *14*, 2584.
- [55] T. A. Berhe, W.-N. Su, C.-H. Chen, C.-J. Pan, J.-H. Cheng, H.-M. Chen, M.-C. Tsai, L.-Y. Chen, A. A. Dubale, B.-J. Hwang, *Energy Environ. Sci.* **2016**, *9*, 323.
- [56] A. A. Mamun, Y. Mohammed, T. T. Ava, G. Namkoong, A. A. Elmustafa, *Mater. Lett.* **2018**, *229*, 167.
- [57] A. Alberti, C. Bongiorno, E. Smecca, I. Deretzis, A. La Magna, C. Spinella, *Nat. Commun.* **2019**, *10*, 2196.
- [58] M. Saliba, *Science* **2018**, *359*, 388.
- [59] W. Pan, H. Wu, J. Luo, Z. Deng, C. Ge, C. Chen, X. Jiang, W.-J. Yin, G. Niu, L. Zhu, L. Yin, Y. Zhou, Q. Xie, X. Ke, M. Sui, J. Tang, *Nat. Photonics* **2017**, *11*, 726.
- [60] R. Zhuang, X. Wang, W. Ma, Y. Wu, X. Chen, L. Tang, H. Zhu, J. Liu, L. Wu, W. Zhou, X. Liu, Y. Yang, *Nat. Photonics* **2019**, *13*, 602.
- [61] Y. Liu, Y. Zhang, Z. Yang, J. Cui, H. Wu, X. Ren, K. Zhao, J. Feng, J. Tang, Z. Xu, S. (Frank) Liu, *Adv. Optical Mater.* **2020**, *8*, 2000814.
- [62] J. Wu, L. Wang, A. Feng, S. Yang, N. Li, X. Jiang, N. Liu, S. Xie, X. Guo, Y. Fang, Z. Chen, D. Yang, X. Tao, *Adv. Funct. Mater.* **2022**, *32*, 2109149.
- [63] Y. Zhou, L. Zhao, Z. Ni, S. Xu, J. Zhao, X. Xiao, J. Huang, *Sci. Adv.* **2021**, *7*, eabg6716.
- [64] J. Zhao, L. Zhao, Y. Deng, X. Xiao, Z. Ni, S. Xu, J. Huang, *Nat. Photonics* **2020**, *14*, 612.
- [65] H. Zhang, G. Dun, Q. Feng, R. Zhao, R. Liang, Z. Gao, T. Hirtz, M. Chen, X. Geng, M. Liu, Y. Huang, X. Zheng, K. Qin, X. Tan, X. Wang, D. Xie, Y. Yang, H. Tian, Y. Zhou, N. P. Padture, X. Wang, J. Hong, T.-L. Ren, *IEEE Trans. Electron Devices* **2020**, *67*, 3191.
- [66] Y. Song, L. Li, M. Hao, W. Bi, A. Wang, Y. Kang, H. Li, X. Li, Y. Fang, D. Yang, Q. Dong, *Adv. Mater.* **2021**, *33*, 2103078.
- [67] N. Ahn, D.-Y. Son, I.-H. Jang, S. M. Kang, M. Choi, N.-G. Park, *J. Am. Chem. Soc.* **2015**, *137*, 8696.